Turbulence budgets in oblique shockwave/turbulent boundary layer interactions

By B. Morgan AND S.K. Lele

1. Motivation and objectives

In high-speed aerodynamics, shockwave/turbulent boundary layer interactions (STBLIs) can be responsible for design-limiting thermal and pressure loads (Dolling 2001). Additionally, when experienced in the inlet/isolator systems of ramjets and scramjets, separation and flow unsteadiness caused by STBLI can lead to additional blockage effects which may affect operability margins to engine unstart (Wagner *et al.* 2009). It is unclear, however, how accurately STBLIs, which have been shown experimentally to experience low-frequency unsteadiness (Dolling & Murphey 1983), can be captured with Reynolds-averaged Navier-Stokes (RANS) computations (Settles *et al.* 1979; Zheltovodov 2004). It is therefore the objective of the present work to explore the physics of oblique STBLI with high-fidelity large-eddy simulation (LES) and to present accurate descriptions of the turbulence budgets for a variety of interactions with different shock strengths and Reynolds numbers. It is our hope that this information can then be used to better inform reduced-order models such as RANS for predictions of STBLI phenomena.

Previous work by our group (Morgan *et al.* 2011*a*) has presented and established confidence in our LES database of oblique STBLI simulations by comparison with direct numerical simulation (DNS) by Pirozzoli & Bernardini (2011) and experimental particle image velocimetry (PIV) by Piponniau *et al.* (2009). In the present work, we build upon our previous results by compiling turbulence budgets for seven different shock strengths (achieved by varying the shock-generating wedge angle between 6.5° and 9.5°) with baseline results at two different Reynolds numbers (Re_θ = 1500, 2300). In section 2, we begin by presenting a brief discussion of the mathematical formulation, numerical schemes, and flow conditions used in the present study. In section 2.3, the cause and effect of numerical dissipation in our numerics is investigated in some detail, and in section 2.4, we validate our baseline budget by comparison with DNS results by Pirozzoli & Bernardini (2011). Then, in section 3, we present the turbulence budgets extracted from our oblique STBLI database with parametric variation. Finally, in section 4, conclusions are drawn and recommendations are made regarding the direction of future research.

2. Computational setup and validation

2.1. *Mathematical models*

The numerical code used in this study solves the spatially filtered compressible Navier-Stokes equations for an ideal non-reactive gas. A sixth-order compact difference scheme (Lele 1992) is used to solve the governing equations in transformed curvilinear coordinates, and Gauss-Seidel alternate directional implicit factorization (Obayashi *et al.* 1988; Iizuka 2006) is used with three Newton-Raphson sub-iterations for time integration with second-order backwards differencing. At each time step, an eighth-order low-pass spatial filtering scheme (Lele 1992) (with optimization parameter $\alpha_f = 0.495$) is applied once

Refinement Level	Δx^+	Δy^+	Δz^+
L1	50-30-50	1-30	30
L2	30-17-30	1-15	15
L3	25-14-25	1-12.5	12.5
L4	20-11-20	1-10	10

$Re_\theta = \{1500, 2300, 4800\}$

Grid Type	L_x	L_y	L_z
STD	$10\delta_0$	$8.5\delta_0$	$3.0\delta_0$
WIDE	$10\delta_0$	$8.5\delta_0$	$6.0\delta_0$
LONG	$20\delta_0$	$12.5\delta_0$	$3.0\delta_0$

Wedge Angle = {6.5, 7.0, 7.5, 8.0, 8.5, 9.0, 9.5}

How to read a descriptor string:

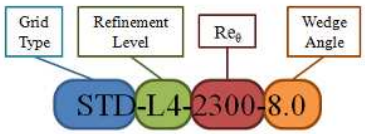

FIGURE 1. A color-coded key to summarize simulation flow conditions and naming conventions. Grid dimensions given are for the interaction mesh only, and regions of stretching are indicated by a dash. Descriptor strings are used to refer to individual simulations without ambiguity.

to the conservative variables to ensure stability, and we utilize second- and fourth-order near-boundary formulas developed by Gaitonde & Visbal (1998) that retain the tridiagonal form of the equation set. In order to maintain time accuracy of the solution, the time step is selected such that the Courant-Friedrichs-Lewy (CFL) number is near, but less than, unity. This choice of time-integration scheme and time-step size should be sufficiently accurate based on the results of our previous work (Kawai *et al.* 2010).

Since central differencing schemes, such as the compact differencing scheme used in the present study, can generate non-physical oscillations in regions of high gradient, a shock capturing scheme is desirable; however, such a scheme must not be so dissipative that it eliminates smaller scales of turbulence. For this reason, the Localized Artificial Diffusivity (LAD) method of shock capturing (Kawai *et al.* 2010) is applied. The method, which is based on Cook's method (Cook 2007) of adding artificial coefficients to the fluid transport terms and improved by modification of Mani *et al.* (2009), is enhanced by the addition of a dilatation-based switching function in the formulation of the artificial bulk viscosity. This switching function removes unnecessary bulk viscosity within expansion and shock-free weakly compressible turbulence regions and allows it to localize only near shocks. Aside from the implicit model created by addition of the artificial bulk viscosity and thermal conductivity, no additional SGS model is used. We have previously assessed the effect of SGS models (Kawai *et al.* 2010), and explicit SGS models with low-pass filtering were found to result in additional damping of the resolved turbulence at similar Reynolds number and grid resolution. Detailed description of the governing equations and the LAD scheme can be found in previous works by our group (Kawai *et al.* 2010; Kawai & Lele 2010, 2008).

2.2. *Parametric variation*

As described by Morgan *et al.* (2011*a*), the LES database utilized in the present study consists of 19 total simulations of oblique STBLI over an adiabatic flat plate with freestream Mach number $M_\infty = 2.28$ and varying grid resolutions, domain sizes, Reynolds

numbers, and wedge angles. In all simulations, periodic boundary conditions are applied in the spanwise direction, and recycling/rescaling with dynamic reflection (RR+DR) (Morgan *et al.* 2011*b*) is used to generate the inflow turbulence. RR+DR represents a variation of the traditional recycling/rescaling method for compressible boundary layers developed by Urbin & Knight (2001) in which the recycled profile is first reflected about a temporally dynamic spanwise location. This method has been shown to eliminate spurious spatiotemporal correlations associated with the recycling frequency without damaging the physical structure of the turbulence (Morgan *et al.* 2011*b*). As described by Morgan *et al.* (2011*a*), our approach is to simulate an undisturbed turbulent boundary layer simultaneously and in a separate mesh from the interaction. The recycled profile is then extracted and imposed as inflow conditions to the interaction mesh. For this reason, the upstream boundary layer thickness δ_0 is evaluated at the inlet of the interaction mesh (and is equivalent to the capture plane in the undisturbed boundary layer simulation). The farfield boundary opposite the adiabatic wall is a buffer region and is high enough such that all disturbances exit through a simple extrapolation outflow. In the interaction mesh, above the incoming boundary layer, Rankine-Hugoniot relations are used to specify freestream values before and after the shock at the inlet plane. In the case of wedge angle variations, the height of the shock on the inlet plane is varied such that the inviscid shock impingement point (that is, the point at which the oblique shock would impinge on the flat plate in the absence of a boundary layer), x_0, is kept constant.

Figure 1 summarizes the various simulations undertaken and establishes the notation by which simulations will be referred in the remainder of this study. Note that the values in Figure 1 are a priori estimations; due to variations in incoming boundary layer properties, resolutions and Reynolds numbers vary slightly from these values. Tables A1 and A2 in the Appendix of Morgan *et al.* (2011*a*) provide detailed flow conditions and grid data, respectively, for each of the 19 simulations computed. Flow conditions are chosen to be generally comparable to DNS by Pirozzoli & Bernardini (2011) ($M_\infty = 2.28$, $Re_\theta = 2300$, $\phi = 8°$) and experiment by Piponniau *et al.* (2009) ($M_\infty = 2.28$, $Re_\theta = 5100$, $\phi = 7 - 9.5°$).

2.3. *Numerical dissipation*

As described previously, the numerical code used in the present study employs an eighth-order, spatial filtering scheme (Lele 1992) (with optimization parameter $\alpha_f = 0.495$) once per time step to ensure stability. Unless the spatial resolution is very high, however, the effect of this filtering can be to dissipate turbulence kinetic energy (TKE), which may adversely impact the resolved TKE budget. Fortunately, we can quantify the numerical dissipation due to filtering by computing TKE before and after the filtering step. In this section, we investigate the role that numerical dissipation may play by considering the TKE budget for an undisturbed turbulent boundary layer at various levels of grid resolution. Each simulation in this section is performed with $M_\infty = 2.28$, $Re_\theta = 2300$, and non-dimensional time step $\Delta\tau = 0.0006$ (CFL ≈ 0.5). The transport equation for TKE ($k = \widetilde{u_i'' u_i''}/2$) is given in compressible form in eq. 2.1 (Pirozzoli *et al.* 2004).

$$\frac{\partial \overline{\rho} k}{\partial t} = C_k + T_k + P_k + V_k + K_k + D_k. \tag{2.1}$$

In the above equation, C_k, T_k, P_k, V_k, D_k, and K_k represent, respectively, terms due to convection, turbulent transport, production, viscous diffusion, dissipation, and compressibility effects. Explicitly, these terms are given by eqs. 2.2 through 2.4. In these

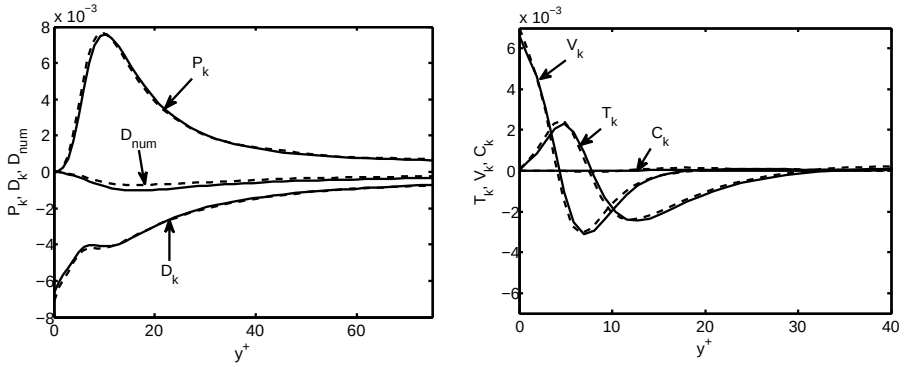

FIGURE 2. Effect of grid resolution on TKE budget in undisturbed boundary layer. Normalization by freestream density, freestream velocity, and local boundary layer thickness. Solid lines: STD-L2-2300-8.0. Dashed lines: STD-L4-2300-8.0.

equations, ρ indicates density, t indicates time, x_j indicates spatial dimension, u_j indicates the velocity vector, p indicates pressure, and σ_{ij} indicates the viscous stress tensor. An overbar is used to denote Reynolds averaging, a tilde denotes Favre averaging, and a circumflex denotes a quantity computed on the filtered field.

$$C_k = -\frac{\partial \widetilde{\overline{\rho} u_j} k}{\partial x_j}, \quad P_k = -\overline{\rho} \widetilde{u_i'' u_j''} \frac{\partial \widetilde{u}_i}{\partial x_j}, \quad V_k = \frac{\partial}{\partial x_j}\left(\overline{\sigma_{ij}' u_i''}\right). \tag{2.2}$$

$$T_k = -\frac{\partial}{\partial x_j}\left[\tfrac{1}{2}\overline{\rho} u_i'' \widetilde{u_i'' u_j''} + \overline{p' u_j''}\right], \quad K_k = \overline{p' \frac{\partial u_i''}{\partial x_i}} + \overline{u_i''}\left(\frac{\partial \overline{\sigma}_{ij}}{\partial x_j} - \frac{\partial \overline{p}}{\partial x_i}\right). \tag{2.3}$$

$$D_k = D_{res} + D_{num} = \left[-\overline{\sigma_{ij}' \frac{\partial u_i''}{\partial x_j}}\right] - \left[\frac{\rho_\infty}{\Delta \tau}\left(\widehat{\overline{k}} - \overline{k}\right)\right]. \tag{2.4}$$

Note that we define total dissipation, D_k, as the sum of the resolved dissipation, D_{res}, and the numerical dissipation, D_{num}. In this case, we assume that all of the numerical dissipation is due to filtering. To assess the effect numerical dissipation on the budget, we plot in Figure 2 the TKE budget terms for two levels of grid resolution (L2 and L4). While it is clear that increasing the grid resolution decreases the peak $|D_{num}|$, total dissipation and production do not seem to be significantly changed. There may be some effect on the peak turbulent transport very near the wall; however, beyond $y^+ \approx 25$, there appears to be no difference between the two levels of refinement. Therefore, we conclude that grid resolution levels L2 and above are sufficient to appropriately resolve TKE production, with numerical dissipation due to filtering effectively acting as a subgrid model of dissipation at un-resolved scales. Note that values of K_k are not plotted in Figure 2 because they are essentially negligible.

2.4. *Baseline comparison with DNS*

Before presenting the effect of our parametric variation on the turbulence budgets, we first seek to assess the quality of our baseline solution by comparison with existing DNS data (Pirozzoli & Bernardini 2011). The comparison DNS results were obtained using a hybrid central-differencing/5th-order weighted-essentially nonoscillatory (WENO) discretization with no filtering and switching controlled by a modified Ducros sensor. In Figures 3 and 4, we plot the budget terms at two different streamwise locations in the interaction. First,

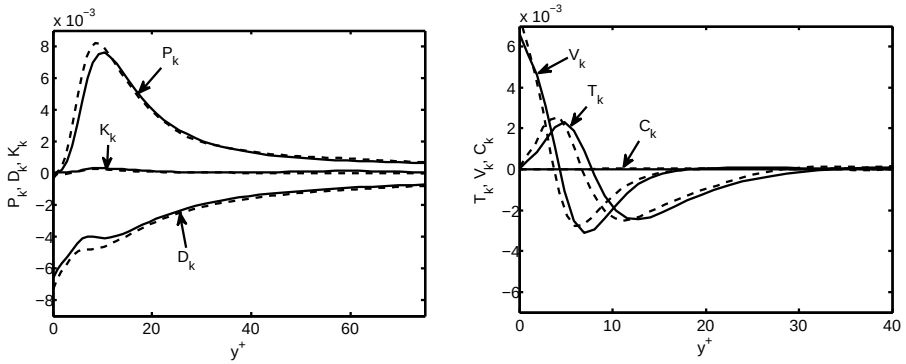

FIGURE 3. Comparison of baseline (STD-L2-2300-8.0) TKE budget with DNS by Pirozzoli & Bernardini (2011) at $(x-x_0)/\delta_0$ = -5.58. Normalization by freestream density, freestream velocity, and local boundary layer thickness. Solid lines: present LES. Dashed lines: Pirozzoli DNS.

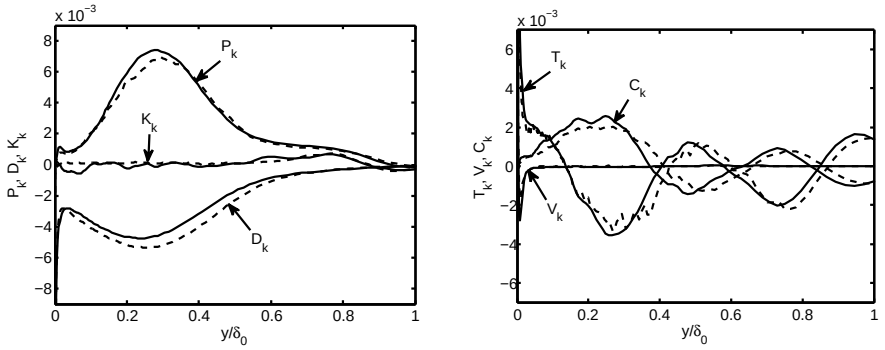

FIGURE 4. Comparison of baseline (STD-L2-2300-8.0) TKE budget with DNS by Pirozzoli & Bernardini (2011) at $(x-x_0)/\delta_0$ = -0.14. Normalization by freestream density, freestream velocity, and local boundary layer thickness. Solid lines: present LES. Dashed lines: Pirozzoli DNS.

the budget at 5.58 boundary layer thicknesses upstream of the inviscid shock impingement point is plotted in Figure 3. We see that while there are some minor discrepancies in the location and magnitude of peak quantities, the budgets generally agree quite well. Next, we consider the TKE balance through the separation bubble by plotting in Figure 4 the budget terms at only 0.14 boundary layer thicknesses upstream of the inviscid shock impingement point. While both the LES and DNS data are somewhat noisier, we again see generally good agreement despite what appears to be a shifting trend towards the left in the LES turbulent transport and convective components. This may indicate that the average height of the separation bubble is somewhat less in the LES. Despite the differences that are observed, however, the present LES is found to be in generally good agreement with the DNS, which provides confidence in the use of our numerics for exploring the effect of wedge angle (shock strength) on turbulence budgets where no DNS data are available.

3. Results

Having established in the previous section that our baseline results at grid resolution level L2 are sufficient to accurately capture the TKE budget in both the undisturbed boundary layer and interaction regions, we now turn our attention towards the effect of

shock strength on the various budget terms. In addition to the TKE budget described earlier by eq. 2.1, we also consider the Navier-Stokes momentum and energy equations, reproduced in eqs. 3.1 and 3.2 as they were presented by Huang *et al.* (1995). Note that we do not here consider the mass continuity equation because this equation contains no unclosed turbulence terms. In eq. 3.2, e represents the internal energy, q_j represents the heat-flux vector, k represents the turbulence kinetic energy for which the expression was given in section 2.3, K represents the mean-flow kinetic energy ($K = \widetilde{u}_i\widetilde{u}_i/2$), $K'' = \widetilde{u}_i u_i''$, and $k'' = u_i''u_i''/2 - \widetilde{u_i''u_i''}/2$.

$$\frac{\partial}{\partial t}\left(\overline{\rho}\widetilde{u}_i\right) = -\frac{\partial}{\partial x_j}\left(\overline{\rho}\widetilde{u}_i\widetilde{u}_j\right) - \frac{\partial \overline{p}}{\partial x_i} + \frac{\partial}{\partial x_j}\left(\overline{\sigma}_{ij} - \overline{\rho}\widetilde{u_i''u_j''}\right). \tag{3.1}$$

$$\begin{aligned}\frac{\partial}{\partial t}\overline{\rho}\left[\widetilde{e} + K + k\right] = &-\frac{\partial}{\partial x_j}\overline{\rho}\widetilde{u}_j\left[(\widetilde{e} + \overline{p}/\overline{\rho}) + K + k\right] + \frac{\partial}{\partial x_j}\left(\overline{\sigma}_{ij}\overline{u}_i + \overline{\sigma'_{ij}u'_i} - \overline{q}_j\right) \\ &-\frac{\partial}{\partial x_j}\left(\overline{\rho}\widetilde{u_j''K''} + \overline{\rho}\widetilde{u_j''k''} + c_p\overline{\rho}\widetilde{u_j''T''}\right).\end{aligned} \tag{3.2}$$

In the following subsections, we present budget profiles for the streamwise momentum, wall-normal momentum, total energy, and turbulence kinetic energy equations with normalization by freestream density, freestream velocity, and local boundary layer thickness. These results are presented for simulations at seven different wedge angles (shock strengths), from simulations STD-L2-1500-6.5 through STD-L2-1500-9.5. Profiles are presented at two different streamwise locations within the interaction, corresponding to points both upstream and downstream of the impinging shock foot. When selecting the location for comparison, the streamwise dimension is scaled by the interaction length, L_{int}, which is found by extrapolating the location of the reflected shock foot to the wall and computing the distance to this point from x_0. This scaling ensures a fair comparison among the various wedge angles since L_{int}/δ_0 varies between 2.62 and 3.81 as wedge angle is increased from 6.5° to 9.5°.

3.1. *Momentum conservation budgets*

Denoting the right-hand side terms in eq. 3.1 (moving from left to right) by C, P, V, and T, which indicate, respectively, the contributions due to convection, pressure, viscous diffusion, and turbulent transport, we now plot in Figure 5 the streamwise and wall-normal momentum budgets at $(x - x_0)/L_{int}$ = -0.60 and 0.00. First, by considering the streamwise momentum budgets, we observe that all four terms are active in the inner boundary layer region, with the greatest contribution due to turbulent transport and the viscous contribution approaching zero around $y/\delta_0 \approx 0.08$. It is also interesting to note that upstream of the impinging shock foot, there is a trend of increasing magnitude with increasing shock strength, while downstream this trend reverses. This may seem somewhat counter-intuitive at first; however, it is likely a result of the shock foot being closer to the wall in the case of the smaller wedge angle. That is, greater wedge angles create greater separation, which results in the sonic line rising away from the wall with increased wedge angle. Thus, we see at $(x - x_0)/L_{int} = 0.00$, terms related to total stress (viscous stress + Reynolds stress) balance the pressure gradient near the wall, and we know that this total should be greater for smaller wedge angles due to faster downstream recovery rates, as shown by plots of skin friction in Morgan *et al.* (2011*a*). In the wall-normal accounting, however, the viscous term is negligible, and the convective and turbulent

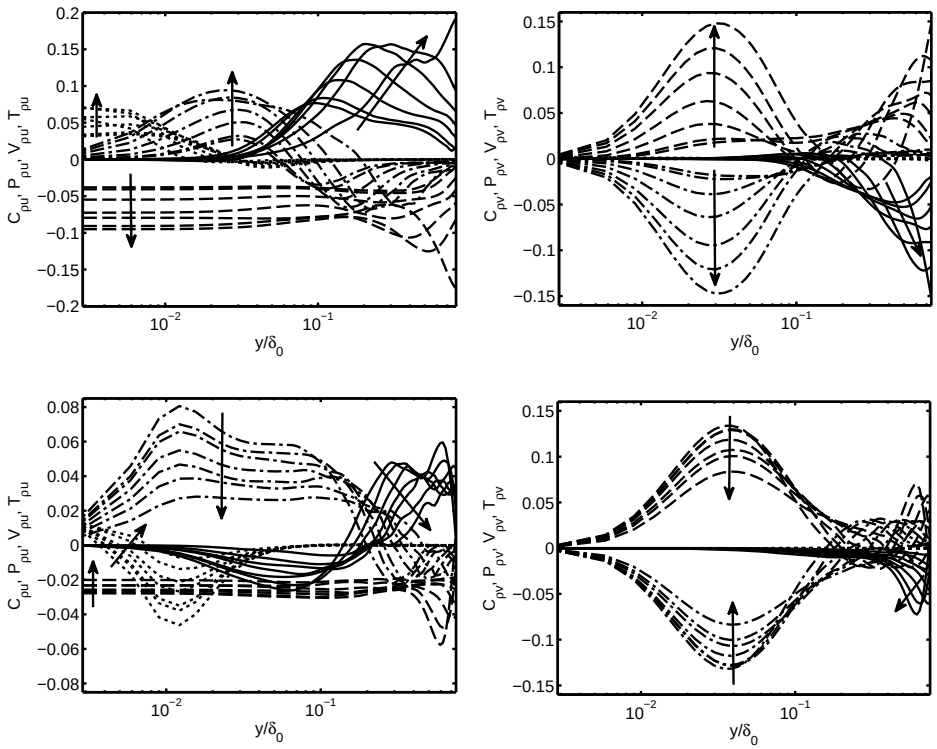

FIGURE 5. Change in momentum budget terms as a function of wedge angle. (Left) Streamwise momentum. (Right) Wall-normal momentum. (Top) $(x - x_0)/L_{int}$ = -0.60. (Bottom) $(x - x_0)/L_{int} = 0.00$. Arrows indicate direction of *increasing* wedge angle from 6.5° to 9.5°. Solid: C; dashes: P; dots: V; dashes and dots: T.

transport terms balance each other for most of the boundary layer thickness, with the convective term playing a role only near the shock.

3.2. *Energy conservation budgets*

We now consider the energy conservation budget described by eq. 3.2. Notice that the right-hand terms in this equation are grouped into three divisions, indicating, respectively, the convective term, contributions from molecular diffusion, and contributions from turbulent diffusion. For convenience, let us denote the entire convective term by C_E. We then denote the molecular diffusion terms, moving left to right, by $V1_E$, $V2_E$, and Q_E, which indicate, respectively, the contributions due to viscous diffusion and molecular heat flux. Finally, we denote the turbulent diffusion terms, moving left to right, by $T1_E$, $T2_E$, and H_E, indicating, respectively, contributions associated with mean-flow kinetic energy, turbulence kinetic energy, and turbulent enthalpy flux.

In Figure 6, we plot the various terms in the energy budget for our seven values of increasing wedge angle. Note that to ease in visualization, we have plotted the convective term and molecular diffusion terms separately from the turbulent diffusion terms. Despite some noise in the convective term, we are able to again identify in the same trends regarding magnitude and wedge angle. That is, in the upstream location, we generally see terms increasing in magnitude with increased wedge angle, whereas this trend is reversed

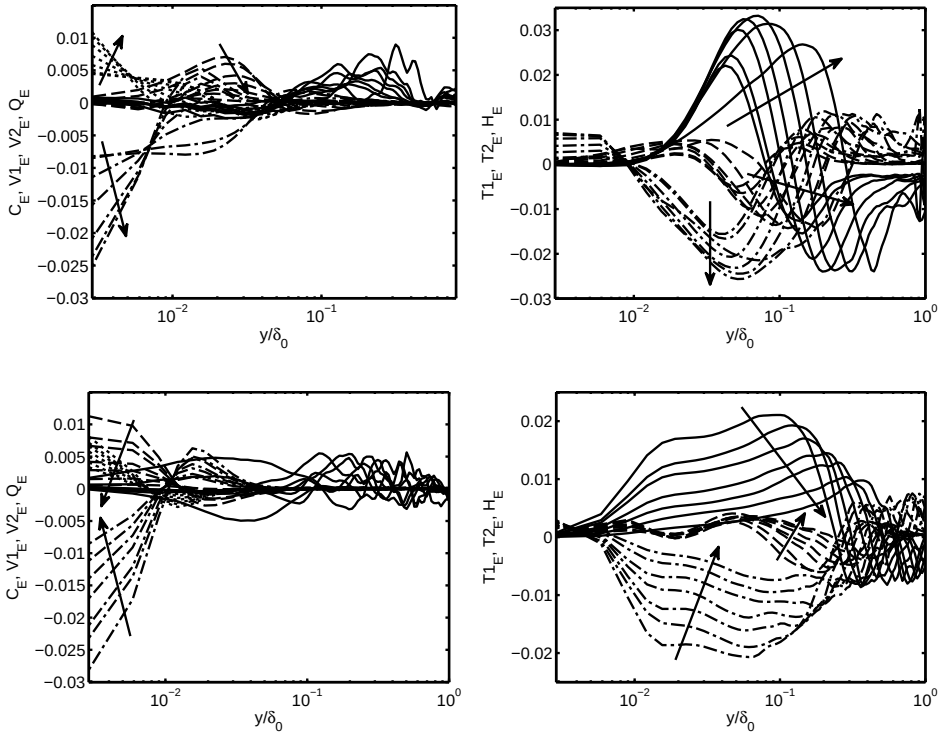

FIGURE 6. Change in energy budget terms as a function of wedge angle. (Left) Convection and molecular diffusion terms. Solid: C_E; dashes: $V1_E$; dots: $V2_E$; dashes and dots: Q_E. (Right) Turbulent diffusion terms. Solid: $T1_E$; dashes: $T2_E$; dashes and dots: H_E. (Top) $(x - x_0)/L_{int}$ = -0.60. (Bottom) $(x - x_0)/L_{int} = 0.00$. Arrows indicate direction of *increasing* wedge angle from 6.5° to 9.5°.

at the downstream location. Additionally, we see that while the molecular diffusion terms appear to be significant very near the wall, none of the molecular diffusion terms are observed to be significant outside $y/\delta_0 \approx 0.05$. By contrast, we see that the turbulent diffusion terms contribute the most above $y/\delta_0 \approx 0.02$. In the downstream location, the term associated with mean-flow kinetic energy, $T1_E$, appears to approximately balance the turbulent heat flux, H_E, up to $y/\delta_0 \approx 0.1$, while in the upstream location, all three turbulent diffusion terms contribute significantly.

3.3. *Turbulence kinetic energy budgets*

Turning now to the turbulence kinetic energy budget described by eq. 2.1, we plot in Figure 7 the variation in TKE terms with increasing wedge angle. As we have done previously, the terms are divided into two plots for clarity, with contributions from production (P_k), dissipation (D_k), and compressibility (K_k) illustrated separately from contributions due to turbulent transport (T_k), viscous diffusion (V_k), and convection (C_k). Again, we see the familiar trend of increasing magnitude with wedge angle at the upstream location and decreasing magnitude downstream. We also notice that in the inner boundary layer, all terms except convection appear to contribute significantly to the budget. The convective term appears to be important only in the outer boundary layer (and in fact changes signs between the upstream and downstream locations), whereas the viscous diffusion

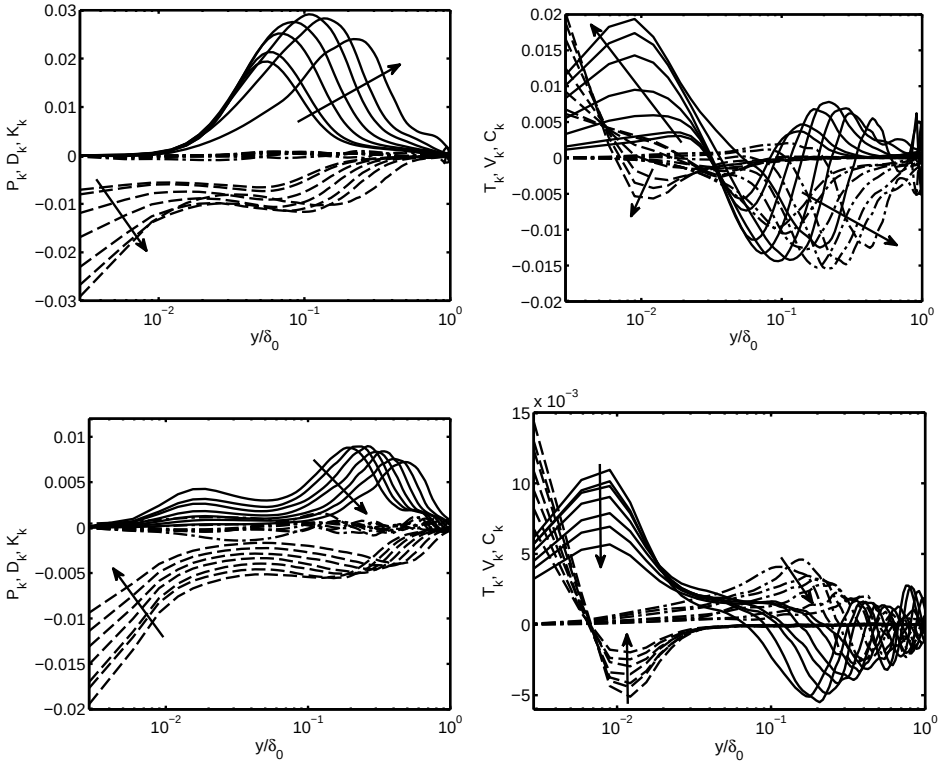

FIGURE 7. Change in turbulence kinetic energy budget terms as a function of wedge angle. (Left) Solid: P_k; dashes: D_k; dashes and dots: K_k. (Right) Solid: T_k; dashes: V_k; dashes and dots: C_k. (Top) $(x-x_0)/L_{int}$ = -0.60. (Bottom) $(x-x_0)/L_{int} = 0.00$. Arrows indicate direction of *increasing* wedge angle from 6.5° to 9.5°.

term appears to be important only in the inner boundary layer. Additionally, while there appears to be some noise in the contribution due to compressibility terms, it appears that K_k is generally small enough to be disregarded as negligible. By comparing our STD-L2-1500-8.0 results with the baseline STD-L2-2300-8.0 results, we observe that the effect of increasing Reynolds number is to generally increase the peak magnitudes while simultaneously shifting the location of peak values closer to the wall.

If we now look at mean TKE production in two dimensions (recalling that the simulation is periodic in the spanwise direction), as in Figure 8, there are a few more interesting observations that can be made. First, we notice, as indicated by the solid black line in this figure, that there is a small region behind the incident shock and below the reflected shock over which the sign of the production term is negative; this feature appears to be associated with the expansion fan originating from the top of the separated flow region. In fact, for a simple shear flow interacting with a normal shock, rapid distortion theory predicts that we should see such a region (Mahesh *et al.* 1994). By also plotting in Figure 8 the TKE budget for the STD-L2-1500-8.0 simulation at a location that passes through this region of negative production, we are able to see that when the production is negative, it is balanced mostly by compressibility terms (where pressure dilatation, in particular, contributes the most to K_k). We additionally see that the shock crossing location appears to move upstream and away from the wall with increased wedge angle.

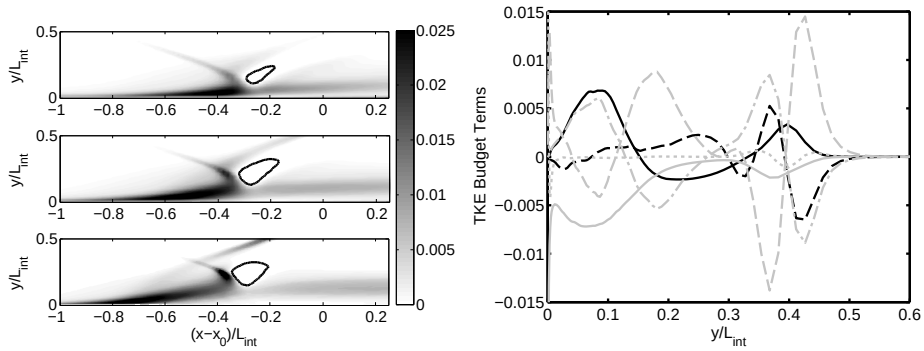

FIGURE 8. (Left) Contours of mean TKE production for wedge angle increasing top to bottom (6.5°, 8.0°, & 9.5°). Solid black line indicates region of negative production (P_k = -0.001). (Right) TKE budget taken in 8° baseline solution through region of negative production at $(x-x_0)/L_{int}$ = -0.25. Solid black: P_k; dashed black: K_k; solid gray: D_k; dashed gray: T_k; dotted gray: V_k; gray dashes and dots: C_k.

4. Conclusions

In this study, we have utilized the LES parametric database of oblique shock/turbulent boundary layer interaction previously described by Morgan *et al.* (2011*a*) to extract and investigate the effect of wedge angle and Reynolds number on the resolved turbulence budget terms. To establish confidence in our baseline results, in section 2.3, we first sought to describe the role of numerical dissipation in our calculations. Although it was found that the filtering operation introduced unwanted numerical dissipation, it was determined that grid resolution levels L2 and higher were sufficient to resolve TKE production – proving that the numerical dissipation due to filtering serves essentially as a subgrid model of dissipation without causing significant damage to the turbulence budgets. By then comparing TKE budget terms with available DNS data in section 2.4, we established confidence in our baseline solution by demonstrating good agreement in both the upstream and interaction regions for all terms in the TKE budget.

We next sought to investigate the effect of shock strength on the various terms in momentum, energy, and turbulence kinetic energy budgets. For each equation, budget terms were plotted for the seven available wedge angles (varying from 6.5° to 9.5° in intervals of 0.5°) at streamwise stations upstream and downstream of the incident shock foot. In the streamwise momentum budget, it was observed that at the upstream station, the magnitude of budget terms tended to increase with increasing wedge angle, while downstream this trend was reversed. While somewhat counter-intuitive, this observation may be explained by the penetration depth of the incident shock, which extends deeper in the case of a weaker shock. In the wall-normal momentum budget, it was found that only contributions due to pressure gradient and turbulent transport are important in most of the boundary layer. The energy budget illustrated that while contributions due to molecular diffusion are important close to the wall, those due to turbulent diffusion are most important elsewhere. Finally, by plotting the TKE budget terms, we again observed a trend increasing magnitude upstream and decreasing magnitude downstream with increasing wedge angle. By plotting two-dimensional contours of TKE production, we were able to confirm this observation and identified a small region of flow associated with the expansion fan in which the sign of the TKE production is actually negative.

While previous studies (Pirozzoli & Bernardini 2011) have provided information about

turbulence budget accounting in STBLI configurations, very limited data have yet been published to describe how the role of turbulence may change in a systematic way when there is uncertainty in configuration parameters. It is therefore our hope that by investigating the effect of wedge angle variation on the various turbulence budget terms, as we have done in the present study, we can provide data which may be used to better inform reduced-order models such as RANS for predictions of STBLI phenomena. For instance, by providing data identifying the effect of wedge angle variation, we can identify regions that may be sensitive to aleatory uncertainties. Similarly, by providing information on the relative importance of turbulence, we can identify regions that may be sensitive to epistemic uncertainties due to RANS model formulation. The present work, therefore, represents an important step in the description of a high-fidelity database which will be used in future work to specifically identify regions in reduced-order models which are expected to be most sensitive to uncertainty.

Acknowledgments

This research was conducted with government support under and awarded by DoD, AFOSR, NDSEG Fellowship, 32 CFR 168a and by the DoE PSAAP Program. Computer time has been provided by NASA NAS, HPCC at LLNL, and HPC at LANL. We would also like to recognize Dr. M.R. Visbal at AFRL for providing the FDL3DI code that has been extended and used in the present study.

REFERENCES

Cook, A. 2007 Artificial fluid properties for large-eddy simulation of compressible turbulent mixing. *Phys. Fluids* **19** (5), 055103.

Dolling, D. S. 2001 Fifty years of shock-wave/boundary-layer interaction research: What next? *AIAA J.* **39** (8), 1517–1531.

Dolling, D. S. & Murphey, M. 1983 Unsteadiness of the separation shock wave structure in a supersonic compression ramp flowfield. *AIAA J.* **20** (12), 1628–1634.

Gaitonde, D. & Visbal, M. 1998 High-order schemes for Navier-Stokes equations: Algorithm and implementation into FDL3DI. *Tech. Rep.*. Air Force Research Laboratory, AFRL-VA-WP-TR-1998-3060.

Huang, P., Coleman, G. & Bradshaw, P. 1995 Compressible turbulent channel flows: Dns results and modeling. *J. Fluid Mech.* **305**, 185–218.

Iizuka, N. 2006 Study of Mach number effect on the dynamic stability of a blunt re-entry capsule. PhD thesis, University of Tokyo, Tokyo.

Kawai, S. & Lele, S. 2008 Localized artificial diffusivity scheme for discontinuity capturing on curvilinear meshes. *J. Comput. Phys.* **227** (22), 9498–9526.

Kawai, S. & Lele, S. 2010 Large-eddy simulation of jet mixing in supersonic crossflows. *AIAA J.* **48** (9), 2063–2083.

Kawai, S., Shankar, S. & Lele, S. 2010 Assessment of localized artificial diffusivity scheme for large-eddy simulation of compressible turbulent flows. *J. Comput. Phys.* **229** (5), 1739–1762.

Lele, S. K. 1992 Compact finite difference schemes with spectral-like resolution. *J. Comput. Phys.* **103** (1), 16–42.

Mahesh, K., Lele, S. K. & Moin, P. 1994 The response of anisotropic turbulence to rapid homogeneous one-dimensional compression. *Phys. Fluids* **6** (2), 1052–1062.

Mani, A., Larsson, J. & Moin, P. 2009 Suitability of artificial bulk viscosity for

large-eddy simulation of turbulent flows with shocks. *J. Comput. Phys.* **228** (19), 7368–7374.

Morgan, B., Kawai, S. & Lele, S. K. 2011*a* A parametric investigation of oblique shockwave/turbulent boundary layer interaction using LES. In *41st AIAA Fluid Dynamics Conference and Exhibit*. AIAA, 2011-3430.

Morgan, B., Larsson, J., Kawai, S. & Lele, S. K. 2011*b* Improving low-frequency characteristics of recycling/rescaling inflow turbulence generation. *AIAA J.* **49** (3), 582–597.

Obayashi, S., Fuji, K. & Gavali, S. 1988 Navier-Stokes simulation of wind-tunnel flow using LU-ADI factorization algorithm. *Tech. Rep.*. NASA, TM-100042.

Piponniau, S., Dussauge, J., Debieve, J. & Dupont, P. 2009 A simple model for low-frequency unsteadiness in shock-induced separation. *J. Fluid Mech.* **629**, 87–108.

Pirozzoli, S. & Bernardini, M. 2011 Direct numerical simulation database for impinging shock wave/turbulent boundary-layer interaction. *AIAA J.* **49** (6), 1307–1312.

Pirozzoli, S., Grasso, F. & Gatski, T. 2004 Direct numerical simulation and analysis of a spatially evolving supersonic turbulent boundary layer at M = 2.25. *Phys. Fluids* **16** (3), 530–545.

Settles, G., Fitzpatrick, T. & Bogdonoff, S. 1979 Detailed study of attached and separated compression corner flowfields in high Reynolds number supersonic flow. *AIAA J.* **17** (6), 579–585.

Urbin, G. & Knight, D. 2001 Large-eddy simulation of a supersonic boundary layer using an unstructured grid. *AIAA J.* **39** (7), 1288–1295.

Wagner, J., Yuceil, K., Valdivia, A., Clemens, N. & Dolling, D. 2009 Experimental investigation of unstart in an inlet/isolator model in Mach 5 flow. *AIAA J.* **47** (8), 1528–1542.

Zheltovodov, A. 2004 Advances and problems in modeling of shockwave turbulent boundary layer interactions. In *Proceedings of the International Conference on the Methods of Aerophysical Research*, pp. 149–157. Institute of Theoretical and Applied Mechanics, Novosibirsk, Russia.